4D quantification of alpine permafrost degradation in steep rock walls using a laboratory-calibrated electrical resistivity tomography approach

Riccardo Scandroglio[1], Daniel Draebing[2,3], Maike Offer[1] and Michael Krautblatter[1]

[1]*Chair of Landslide Research, Technical University Munich, Arcisstrasse 21, Munich, 80335, Germany (E-mail: r.scandroglio@tum.de),* [2]*Chair of Geomorphology, University of Bayreuth, Universitätsstraße 30, Bayreuth, 95447, Germany, and* [3]*Department of Physical Geography, Utrecht University, Princetonlaan 8a CB, Utrecht, 3584, the Netherlands*

ABSTRACT

The warming of rock permafrost affects mechanical stability and hydro-cryostatic pressures in rock walls. The coincident decrease in slope stability frequently affects infrastructure by creep and subsidence and promotes the generation of rockfalls and rockslides. The increasing hazard posed by warming permafrost rock walls and the growing exposure of infrastructure and individuals create a demand for quantitative monitoring methods. Laboratory-calibrated electrical resistivity tomography provides a sensitive record for frozen versus unfrozen bedrock, presumably being the most accurate quantitative monitoring technique in permafrost areas where boreholes are not available. The data presented here are obtained at the permafrost-affected and unstable Steintaelli Ridge at 3100 m a.s.l. and allow the quantification of permafrost changes in the longest electrical resistivity tomography time series in steep bedrock. Five parallel transects across the rock ridge have been measured five times each, between 2006 and 2019, with similar hardware. Field measurements were calibrated using temperature-resistivity laboratory measurements of water-saturated rock samples from the site. A 3D time-lapse inversion scheme is applied in the boundless electrical resistivity tomography (BERT) software for the inversion of the data. To assess the initial data quality, we compare the effect of data filtering and the robustness of final results with three different filters and two time-lapse models. We quantify the volumetric permafrost distribution in the bedrock and its degradation in the last decades. Our data show mean monthly air temperatures to increase from $-3.4°C$ to $-2.6°C$ between 2005–2009 and 2015–2019, respectively, while simultaneously permafrost volume degraded on average from 6790 m^3 ($\pm$640 m^3 rock in phase-transition range) in 2006 to 3880 m^3 ($\pm$1000 m^3) in 2019. For the first time, we provide a quantita-

E-mail: r.scandroglio@tum.de

tive measure of permafrost degradation in unstable bedrock by using a temperature-calibrated 4D electrical resistivity tomography. Our approach represents a fundamental benchmark for the evaluation of climate change effects on bedrock permafrost.

Key words: Climate change, ERT, Geohazard, 3D.

INTRODUCTION

The change in global climate at the end of last century is well documented by an increase in air temperature, which is probably the oldest and best recorded environmental parameter (Wanner *et al.*, 1998; Casty *et al.*, 2005; Scherrer *et al.*, 2005; IPCC, 2014). High alpine meteorological stations (e.g., Zugspitze-D, Sonnblick-AT and Jungfraujoch-CH) active for up to 120 years are in agreement and show increasing mean annual air temperatures in the last three decades. Between 2008 and 2017, permafrost boreholes in the European Alps documented a mean annual ground temperature (MAGT) increase in rock walls ranging from 0°C to 1°C per decade (Hock *et al.*, 2019), while global MAGT increase is of 0.19 ± 0.05 °C/decade (Biskaborn *et al.*, 2019).

The ground warming leads to an increase in the active-layer thickness (Gruber, Hoelzle and Haeberli, 2004; Pogliotti *et al.*, 2015) and permafrost degradation (Noetzli *et al.*, 2019). Permafrost warming and degradation decrease the rock-mechanical strength (Mellor, 1973; Krautblatter *et al.*, 2013) and weakens ice-filled joints (Mamot *et al.*, 2018). It is still hard to attribute individual collapse events to permafrost degradation because of geological and hydrological factors preparing progressive rock failure independent of permafrost (Gruber and Haeberli, 2007). However, recently, numerous events were recorded in permafrost-affected critical heights and expositions, where a connection with warming permafrost is very likely (Gruber, Hoelzle and Haeberli, 2004; Huggel, 2009; Pirulli, 2009; Ravanel *et al.*, 2013; Phillips *et al.*, 2017; Walter *et al.*, 2020).

In comparison with the melting of glaciers, the degradation of permafrost is not directly visible in the landscape; therefore, the analysis of permafrost spatial and temporal variability and the assessment of climate change consequences are subject to greater uncertainties (Harris *et al.*, 2003). Long-term observation can help to gain important knowledge, and therefore an increasing number of monitoring sites have been established throughout the Alps and elsewhere during the last decades. Most of these studies apply multi-technique approaches including automated weather stations, boreholes, ground surface temperature and laser scanning. Several studies include 2D electrical resistivity tomography (ERT) time-lapse measurements (Pogliotti *et al.*, 2015; Mollaret *et al.*, 2019; Noetzli, Pellet and Staub, 2019), and only a few (Krautblatter *et al.*, 2010; Keuschnig *et al.*, 2017) are monitoring resistivity in solid and steep bedrock, with interesting results but still at too short a time sequence for climate analysis.

The application of quasi-3D ERT (i.e., closely spaced parallel 2D lines) in periglacial geomorphology is generally sparse and does not include monitoring studies, even if it can provide important insights into subsurface heterogeneity and can help mapping permafrost conditions in a spatially extensive way (Kneisel *et al.*, 2014). Only a few studies have so far successfully investigated the suitability of 3D resistivity imaging for alpine environments with coarse surface material by merging several closely spaced 2D ERT lines (Rödder and Kneisel, 2012; Emmert and Kneisel, 2017; Duvillard *et al.*, 2018). Decade-long 3D resistivity measurements in steep bedrock have not been reported so far. Ground truthing can be gained from borehole temperature measurements (Pogliotti *et al.*, 2015; Emmert and Kneisel, 2017; Mollaret *et al.*, 2019), but this is usually not feasible in steep unstable rock walls. A valid alternative is provided by temperature-resistivity ($T-\rho$) laboratory calibration of bedrock samples from the specific study sites (Krautblatter *et al.*, 2010) and these techniques have been subsequently tested in Arctic and Alpine environments (Siewert *et al.*, 2012; Magnin *et al.*, 2015).

In this study, we present a benchmark in permafrost research, introducing a laboratory-calibrated quasi-3D ERT monitoring (hereinafter '3D') in bedrock with time-lapse inversion and try to answer the following questions. (1) Can laboratory-calibrated 4D ERT provide a robust monitoring of permafrost distribution in steep fractured walls and rock ridges? (2) Can we localize and quantify permafrost evolution over more than a decade? (3) What are the implications of permafrost degradation for rock wall stability?
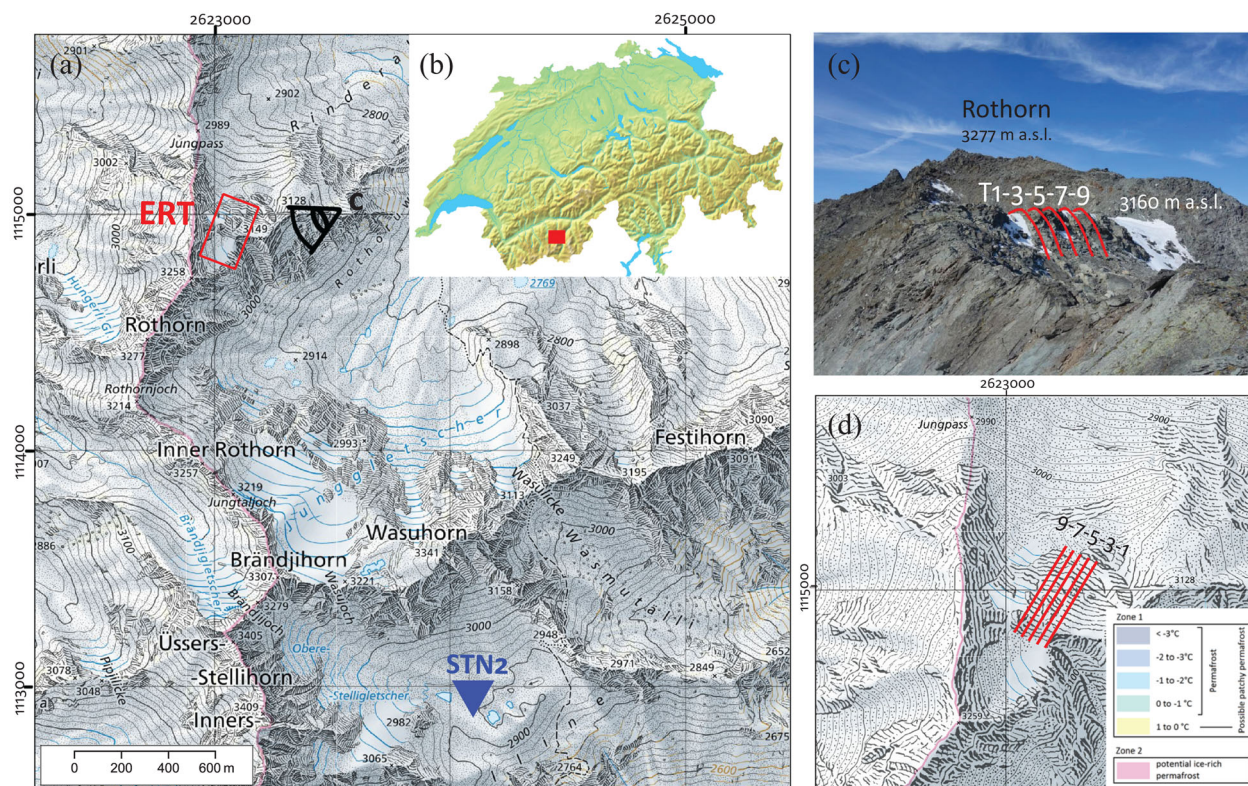
Figure 1 (a) Map of the Steintaelli Ridge (in red; ERT), meteorological station Oberer Stelligletscher (in blue; STN2) and point of view for picture C in black (coordinates in CH103+/LV95, source: © swisstopo; BA20074). (b) Map of Switzerland with highlighted study site (source: Wikipedia). (c) Picture from E–NE with Rothorn peak in the background and the five ERT transects in red. (d) Permafrost and ground ice map from Kenner *et al.* (2019) indicate permafrost occurrence at the Steintaelli.

FIELD SITE

The Steintaelli is located at the crestline between the Matter and Turtmann Valleys in Valais, Switzerland, at an altitudinal range of 3070–3150 m adjacent to the Rothorn (Fig. 1a and b). The lithology in the study area comprises slaty paragneisses with a homogeneous structure. The warming tendency after the Little Ice Age resulted in the massive retreat of the Rothorn NE Glacier, which lost several hundreds of metres of its maximum length. Presently, the remnants of the Rothorn NE Glacier are dissected by newly exposed rock bars in several small ice relics.

All existing permafrost models indicate the occurrence of permafrost in the Steintaelli. The permafrost model by Gruber and Hoelzle (2001) categorizes the northeast side of the ridge as 'possible local permafrost' and 'likely extensive permafrost', while the southwest is categorized as only 'possible patchy discontinuous permafrost'. In contrast, the *Alpine Permafrost Index Map* by Boeckli *et al.* (2012) indicates both expositions as 'permafrost in nearly all conditions' . Similarly,

the model by Kenner *et al.* (2019) also classifies the entire ridge as 'permafrost zone' with an estimated mean annual ground temperature between −1°C and −3°C (Fig. 1d).

Previous geophysical measurements indicated the occurrence of permafrost, especially in the north and east-facing rock walls. Krautblatter and Hauck (2007) conducted, for the first time, 2D electrical resistivity tomography (ERT) in rock walls (starting 2005) and detected permafrost-affected bedrock on the N-slope. ERT data from 2005 to 2007 demonstrated that aggradation in permafrost rocks with and without active cleft water systems evokes significantly different patterns (Krautblatter, 2010). Krautblatter and Draebing (2014) identified permafrost occurrence on the N-slope and ridge along the cross-section using seismic refraction tomography between 2006 and 2007. Draebing *et al.* (2017) monitored active-layer dynamics between 2012 and 2014 and demonstrated a significant influence of snow cover. Long-lasting snow cover reduced significantly any active-layer thawing on the ridge and the north face in 2013 and 2014. Furthermore,
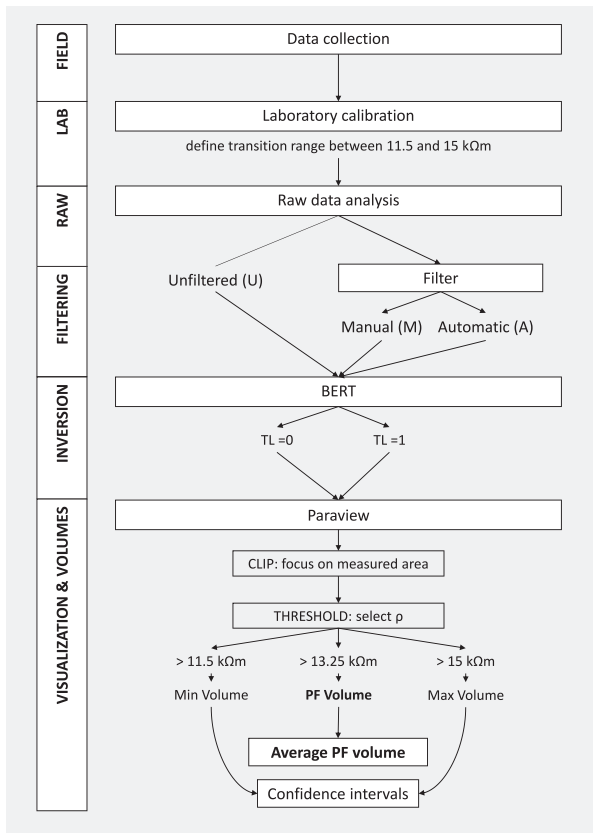
Figure 2 Flowchart of the procedure to obtain permafrost volumes.

Draebing *et al.* (2017) identified cyclical seasonal thermo-cryogenic processes that progressively decrease the stability of the rock wall.

METHODS

The following section presents how meteorological data have been analysed and explains the procedure from field measurements to volume calculation, also presented in the flowchart of Figure 2.

Meteorological data

Meteorological data were obtained from the nearby stations Oberer Stelligletscher STN2 and Platthorn SAA1, both belonging to the Intercantonal Measurement and Information System (IMIS) network and providing simultaneous data since 1999. STN2 is located 2.3 km SE of the Steintaelli at 2914 m a.s.l., while the 9.7 km distant SAA1 is installed at 3245 m a.s.l. By interpolation of their air temperature, we obtained a temperature lapse rate of 0.63°C/100 m

($r^2 = 0.97$), which we applied to model air temperatures for the Steintaelli Ridge.

To highlight annual and seasonal temperature trends, we calculated mean monthly air temperature (MMAT) and its five-year average. We computed mean annual air temperature (MAAT) and its average for the period 1999 to 2009 ($MAAT_{1999–2009}$). The annual difference from this average allowed to highlight years colder and warmer than average. For the final discussion of results, we derived a five-year moving mean of air temperature and compared its long-term fluctuations with changes in apparent resistivity.

Field measurements

In summer 2006, 205 electrodes were drilled on the ridge in five parallel arrays (Fig. 1c), with 41 electrodes each (Krautblatter, 2009). To achieve optimal electrical contact with the rock mass, 10 mm thick and 100 mm long stainless-steel screws were permanently installed and subsequently used as electrodes for our measurements. Electrodes have a minimum spacing of 2 m along the rock surface and the spacing between arrays is 4 m, which is an acceptable distance for 3D applications (Gharibi and Bentley, 2005). Exact electrode positions were measured with tachymeter with approximately 1 cm accuracy. The topographic data were used to create a high-resolution DEM for our inversion process.

Date of measurements, number of data points and instrument settings are summarized in Table 1. Measurements have been conducted between August and September when ground temperatures are expected to be highest and weather or snow conditions enable fieldwork. Before the measurement, we tested the contact resistance of each electrode and excluded electrodes with unrealistic high contact resistances from the measurement. We collected up to 190 data points for each transect with a Wenner array, as this array yields the highest signal-to-noise ratios for mountain permafrost environments (Krautblatter *et al.*, 2010; Rödder and Kneisel, 2012).

Laboratory calibration of the electrical resistivity tomography

Two rock samples with approximate size 20 × 20 × 30 cm and density 2.6 g/cm^3 have been chosen as lithological end members representing the homogeneous lithology of slaty paragneiss in the few decameter large Steintaelli Ridge. Sample S1 has a more enhanced schist structure than S2. Porosity values range from 1.94% ± 0.10% at sample S2

Table 1 Information about field measurements, laboratory calibration and filters

A. Field measurements

	2006	2007	2008	2012	2019
Date	8/8–20/09	10–11/08	2–8/09	18/08	12–13/09
Measurements (out of 950)	948	708	844	835	941
	100%	75%	89%	88%	99%
Instrument (ABEM)		SAS 300		TERRAMETER LS	
Current		0.2–1 mA		0.1–10 mA	
Contact resistance		Mostly <10 kΩm			
Voltage max		800 V		600 V	
Stacks/error		2–4 / 1%			

B. Laboratory calibration

Samples		Sample S1		Sample S2	
device		ABEM SAS 300 TERRAMETER			
Transition range (TR)	11.5–13.5 kΩm		13–15 kΩm		
TR average		11.5–5 kΩm = 13.25 ± 1.75 kΩm			

C. Data filtering

Manual filter rejected		< 2.5 kΩm and > 100 kΩm + manual selection			
	4%	3%	3%	4%	4%
Automatic filter rejected		< 3.2 kΩm and > 63.1 kΩm			
	4%	4%	4%	7%	6%

to 2.4% ± 0.10% at sample S1 (Draebing and Krautblatter, 2012). We installed multiple electrodes with spacing a few cm and depth ~0.5 cm into the middle of the sample surface with the Wenner configuration. In addition, 0.03°C-accuracy calibrated temperature loggers were installed on each rock specimen at the median depth of electric current flow (see, Krautblatter *et al.*, 2010, for details). Samples were submerged in low conductive water (0.032 ± 0.002 S/m) in a closed basin to approach their chemical equilibrium. Pore space was fully saturated under atmospheric pressure and room temperature until resistivity did not decline further (over at least a 24 h period), as free saturation resembles the field situation more closely than saturation under vacuum conditions. We assume 90%–100% saturated pores, which allow the best application of the Archie's law and reflects electrolytic conduction of ion-bearing pore water in long-term chemical equilibrium with the pore wall.

In a freezing chamber, samples were cooled with increments of 0.1–0.2°C in a range of 20°C to −3°C, while continuously monitoring the resistivity using an ABEM SAS 300 TERRAMETER. Ventilation was applied to avoid thermal layering. Samples were loosely coated with plastic film to protect them against drying. A bilinear relationship between temperature and resistivity is expected, with strong differences in the gradient between the frozen and unfrozen state, as already shown by Krautblatter *et al.* (2010). Due to hysteresis effects between freezing–thawing and light resistivity variations between transects, it was not possible to define one single transition point. Therefore, we defined a transition range (TR) of resistivity for each sample: this range includes the end of the supercooling effect of all transects in that sample, even if this point is normally located already under 0°C (Murton *et al.*, 2006, 2016). After this, the two TRs have been united in one single range by taking the minimum and maximum values out of both.

Data pre-processing

Before starting, we calculated geometric factors modelled on the true surface geometry in boundless electrical resistivity tomography (BERT) with the help of a digital terrain model and used those factors to obtain apparent resistivities (ρ_a). In the first step, we analyse differences in time of ρ_a before filtering and inverting the data to exclude their influences in the assessment of changes. To evaluate overall variations in ρ_a,
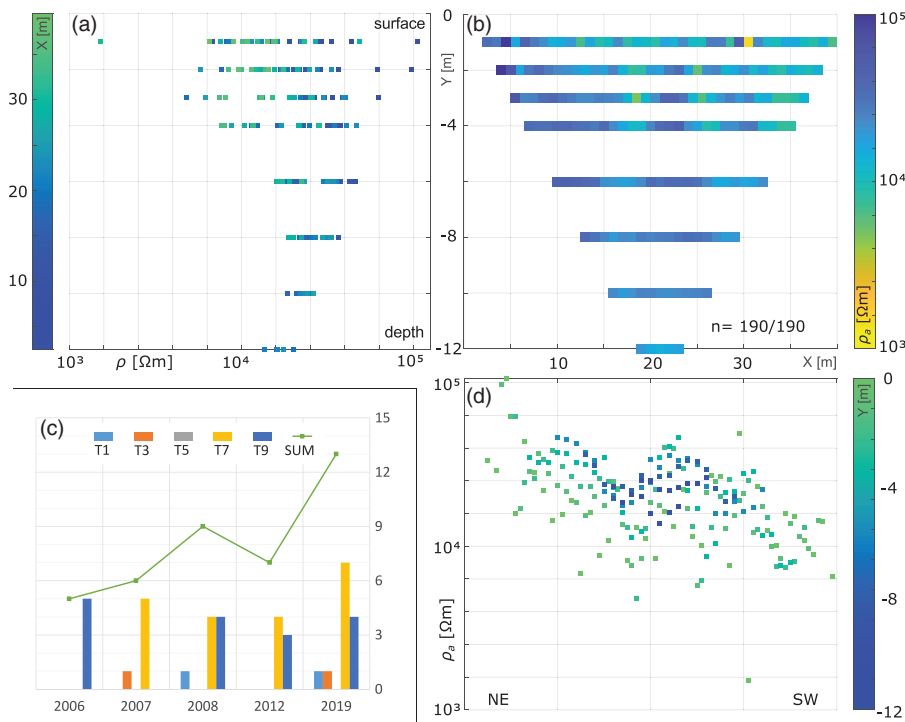
Figure 3 (a) *X* side-view pseudosection, (b) common pseudosection and (d) *y* side-view pseudosection. In (c) the number of measurements that have been manually rejected with side-view pseudosection, displayed by transect and year.

yearly data sets are fitted to a Kernel distribution, plotted as a probability density function (PDF) and compared. Mean values of the PDFs and their percentage changes are numerically analysed. To localize changes in raw data according to depth, quadrupoles from each data set are divided according to electrode distance, namely pseudo-depth (PD). Using Wenner array with electrode distance 2 m, the PD number corresponds approximately to the depth below ground level in metres (e.g., PD = 4 is equal to ∼ 4 m depth). For each PD the average ρ_a is calculated, plotted with others from the same transect, and compared between years.

In the second step, we apply manual (M) and automatic (A) filters to our raw data to exclude outliers and improve the quality of the inversion. We also show results from unfiltered data (U) for evaluating the influence of outliers in volume estimation. In rock permafrost, outliers are most likely caused by insufficient coupling of electrodes, punctual near-surface phenomena like ice- or air-filled crevices or loose scree material. These outliers are characterized by very high or low ρ_a and occur mostly in the active-layer near the surface. Since these phenomena are not the focus of this study, outliers represent a problem for the data fitting of the inversion and therefore need to be removed.

For supporting data filtering, we plotted the raw data in a standard pseudosection and in two 'side-views' graphs, which offer a 3D visualization of the pseudosection. Commonly used pseudosections present differences with colours, but can be easily biased by the chosen scale. The here proposed *side-view pseudosections* (Fig. 3) put resistivity on one axis and the *x* or *y* coordinates on the other. In each side view, the second coordinate can be added by changing marker size or colours. This allows an assessment of resistivity based on simple cartesian coordinates. Large resistivity differences, and thus outliers, are evident because bad data points are located far away from the neighbours.

We used all raw data, including those that were clearly outliers in the unfiltered approach (U). In the manual filtering approach (M), in contrast, we (i) removed extreme low (< 2.5 kΩm) and high values (> 100 kΩm). Then, (ii), we derived side-view pseudosections of apparent resistivity and manually rejected measurements that did not fit with other adjacent data points. If the data points were considered outliers in more than two years, they were eliminated from the whole time series, to allow consistent data filtering over the years. In the third approach, the automatic filtering (A), a range of resistivities were chosen based on the side-view pseudosection

Table 2 BERT parameters for mesh and inversion

Mesh parameters		
SURFACESMOOTH	1	Improves quality of surface grid, making a nicer surface
SURFACEQUALITY	34.7	Quality of the surface mesh, from 35 (good) to 20 (bad)
PRIM3DQUALITY	1.12	Quality of primary mesh, from 1.11 (good) to 2 (bad)
PARA3DQUALITY	1.25	How fast the mesh is growing, from 1.1 (slow) to 2 (fast)
Size of resulting meshes		
ParaMesh – parameter mesh	Nodes: 19,399	Cells: 98,081
Secmesh – secondary mesh	Nodes: 144,305	Cells: 784,648
Inversion parameters		
LAMBDA (λ)	20	Default value in BERT, proved to be appropriate in this case to avoid under- or overfitting
MAX ITER – maximum number of iterations	5	Was selected as fix value to allow better comparison between models. Some calculations would naturally take much more iterations to reach a stopping criterion, but five in the last iterations only little changes happened in the RRMS/χ^2 values
ROBUST DATA	1	For robust (L1) data reweighting
BLOCKY MODEL	1	For contrasts enhancing by robust (L1) methods.
TIME-LAPSE STEP MODEL (also 'TL')	0 or 1	In each frame a full minimization is done, but the models are constrained taking the model of either the first (TL_0) or the preceding (TL_1) frame as reference (Günther and Rücker, 2019)

analysis (3.16–63.1 kΩm), and all values outside this range were excluded.

Data inversion and visualization

For data inversion, we applied the open-source C++/Python-based software BERT due to its capability to deal with the steep ridge-shaped topography and to allow for a real 3D inversion (Günther *et al.*, 2006). BERT is an enhanced code based on existing techniques that combines the fast convergence of regularized Gauss–Newton methods with accurate finite elements forward calculation. It includes a tool for automatic mesh generation and features model discretization by unstructured triangles and tetrahedrons in 2D and 3D, respectively, reaching high topography accuracy and offering a quantification of topographic effects. Forward calculation is very fast thanks to three grids at different coarseness levels: coarse parameter grid, secondary field grid, and highly refined primary field grid. The software allows to choose between the standard smoothness-constrained least-square inversion, which minimizes the squares of the data misfit, and an iteratively reweighted least-square inversion, which is more appropriate for blocky models and more robust with respect to large data differences (expected in the ridge).

In BERT, the regularization parameter λ specifies the weighting between the data misfit Φ_d and model roughness Φ_m (Günther, Rücker and Spitzer, 2006) and, therefore, is a crucial parameter in the inversion process:

$$\Phi = \Phi_d + \lambda\Phi_m \rightarrow \min. \qquad (1)$$

Using large values results in smoothed models with high relative root mean square (RRMS), while using small λ values results in data consistent but very noisy models with low RRMS values (Hauck and Vonder Mühll, 2003). The fitting of the data within errors is expressed by the chi-squared misfit $\chi^2 = \Phi_d/N$, where N is the number of data, and a theoretical value of $\chi^2 = 1$ means a perfect fit of data within the data error. The number of iterations can be decided by the user, but when Φ stagnates or when $\chi^2 \approx 1$ the inversion stops automatically (Günther, Rücker and Spitzer, 2006). During the inversion process, we used two time-lapse approaches: in TL_0, the steps were constrained taking always the first model as reference, while in TL_1 the respective preceding model was used as reference at each time step (Günther and Rücker, 2019). Table 2 presents all the settings for this model.

As shown in Figure 2, we quantified the volume of permafrost using the software Paraview for each time step. We (i) excluded from the mesh not data-determined cells
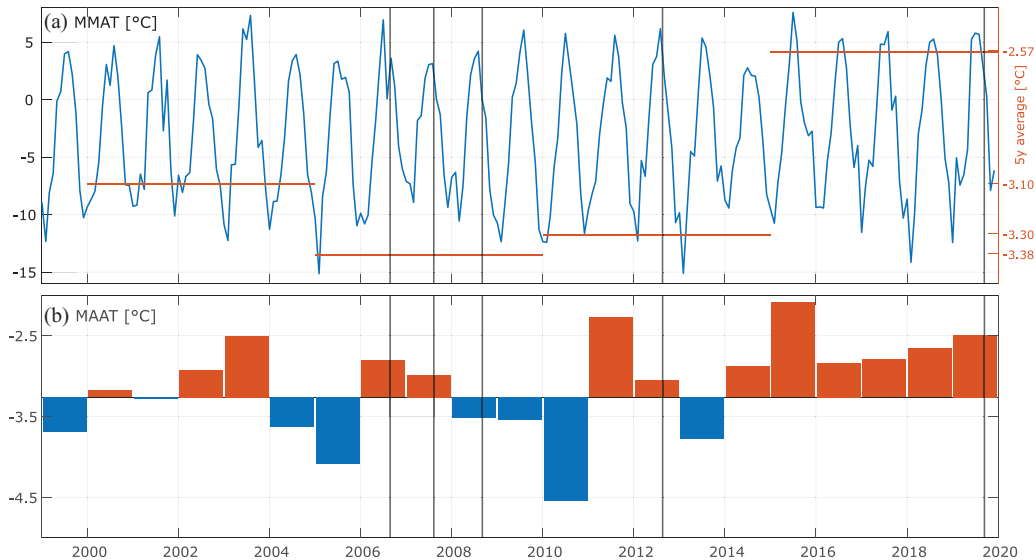
Figure 4 Air temperature from interpolation for the study site. Grey vertical lines show the days when ERT measurements took place. (a) MMAT, with red lines representing the respective five-year averages. (b) MAAT, with base value corresponding to the average of the first 10 years (MAAT$_{1999–2008}$ = −3.26°C).

based on sensitivity and so reduced the volume from 27,434 m^3 to 14,282 m^3. Then we (ii) selected cells that exceeded the thresholds determined in the laboratory calibration (maximum, mean and minimum of transition range) and (iii) calculated total volumes by integration over the selected cells.

RESULTS

Meteorological conditions at the Steintaelli

Mean monthly air temperature (MMAT) revealed higher than average hot summers in 2003, 2006 and 2015, when MMAT ≥ 7°C were recorded at least in one month (Fig. 4a). In addition, the summers of 2003 and 2019 exceeded the 5°C mark for three consecutive months. In winter, MMAT reached −15°C in 2004/05 and 2013/14, while 2006/07 was extremely warm, with a minimum MMAT of only −9°C. The five-year average of MMAT for 2000–2004 is −3.10°C, decreasing to −3.38 °C in 2005–2009 and −3.30°C in 2010–2014. Extraordinary increases of air temperatures in the last five years (2015–2019) raised the average by 0.73°C to the value of −2.57°C.

The mean annual air temperature (MAAT$_{1999–2009}$) was −3.26°C (Fig. 4b). The deviation from MAAT$_{1999–2009}$ revealed that warmer and colder years irregularly alternated and balanced until 2014. From there on, temperatures showed a warmer trend than average without colder years in between.

The warmest years in the analysed period of 21 years were 2015 and 2011, with a MAAT of −2.09°C and −2.27°C, respectively, 1.2°C and 1.0°C above average.

Laboratory resistivity calibration

Calibration results could be accurately fitted by bilinear relations, where freezing occurs with a sudden increase in the $T–\rho$ gradient (Fig. 5). The resistivity range and the $T–\rho$ gradient of frozen and unfrozen samples fit well in the domain of other tested metamorphic rocks in Krautblatter (2009) and references herein. After the supercooling phase, the $T–\rho$ gradient of frozen rock approached average values of 8.7 ± 1.3 kΩm/°C. The transition range (TR) for each sample is highlighted in yellow in Figure 5 and reported in Table 1. These results led to an overall TR of 13.25 ± 1.75 kΩm, whose mean value is used hereafter to estimate permafrost volumes.

Quality assessment of pre-processing and inversions

Probability density functions (PDFs) of raw data clearly showed that ρ_a distributions are shifting with time in the direction of lower values (Fig. 6a). The majority of raw data ranged from 2.5 kΩm to 50 kΩm, values that fit very well with the results of sample calibration. The years 2006 to 2008 show analogous mode, differing slightly in variance and skewness. In comparison, 2012 shows a definite reduction of the mode, and
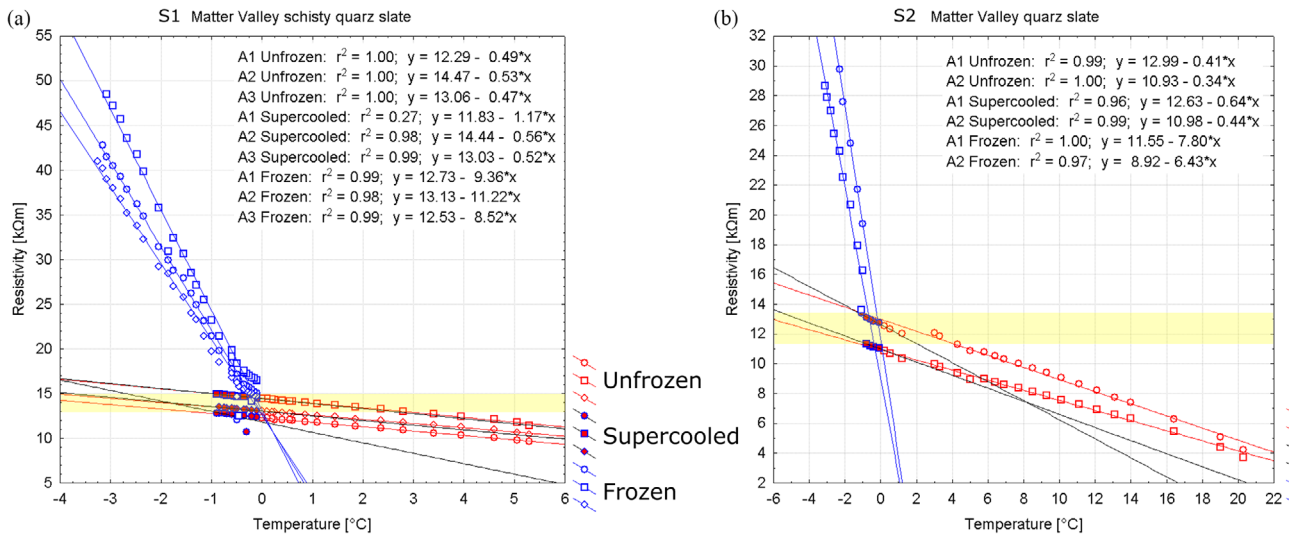
Figure 5 Laboratory results of (a) sample S1 (schisty quartz slate) and (b) sample S2 (quartz slate). Multiple lines represent different quadrupoles in the same sample. Yellow area highlights the range of phase transition that was used to calculate permafrost volumes.

this reduction was even stronger in 2019. The variance was higher in 2012 than in 2019, with a marked negative skewness around 31.5 kΩm in 2012, while in 2019 values were more symmetrical and concentrated close by the mode. The mean revealed minimal decreases of 1% and 2% in 2007 and 2008 (Table 3), respectively, values are considered within the precision of the measurement. On the contrary, a strong reduction of 20% was recorded in 2012 and confirmed with 23% decrease in 2019. Mean PDF values range from 11.6 kΩm to 8.9 kΩm.

In Figure 6(b), the superficial layers (pseudo-depth (PD) ≤ 4) of all transects presented small absolute differences between years in mean ρ_a with fluctuating sign and only seldom a decrease, which corresponded well to active layer's dynamic and its dependency on seasonal conditions. In contrast, mean ρ_a showed an unambiguous decreasing trend at depth (PD > 4). Between 2006 and 2008 only small changes were visible and all the PD had a mean $\rho_a > 10$ kΩm. However, in 2012 and 2019 the decrease is evident, resulting in $\rho_a \leq 10$ kΩm almost everywhere. A clear exception is given by the outlier in the transect T3 at PD = 12 m in 2019, which reached 15.8 kΩm.

Manual filtering rejected on average 3%–4% of the measurements, the automatic filter up to 7%: both values were objectively very low (Fig. 6c). Concerning data fitting, relative root mean square (RRMS) was very variable for unfiltered data (U), fluctuating between 20% and 589%, while for manual filtering (M) and automatic filtering (A) values were limited to 16%–24%. Filter A produced better RRMS in 2007

and 2019 compared with M, which can be explained with 1%–2% more rejected data. In contrast, no significant improvement of RRMS was recorded in 2012, even if 3% more data had been excluded.

Improvements with TL_1 were evident on the RRMS and led to average decreases of 2%, reaching the minimum RRMS of 13% for A_1 in 2012 and 14% for M_1 in 2009. In contrast to the high RRMS in 2012, no significant differences of χ^2 were recorded between years with unfiltered data, with results varying from 5 to 10. With filters A and M, χ^2 values were on average 1–2 points better than with the unfiltered data. Applying the model TL_1 reduced χ^2 a further one point on average, but, as expected, only from the third iteration the time-lapse strategy differs from TL_0.

4D electrical resistivity tomography

The 3D inversions revealed in 2006 a well-defined elongated high-ρ (32 kΩm) body starting at $z = 50/60$ m under the NE slope (Fig. 7). This body developed without interruptions parallel to the slope and grew its depth from 10 to 20 m going from $x = 0$ to 16 m. This was interpreted as a frozen area, apparently connected to the surface of the ridge at $x = 12$–16 m. High ρ at $z = 50$ m were still present in 2007 but a reduction of ρ can be seen at $z = 40$–45 m along a corridor perpendicular to the slope in $x = 0$, 4 and 8 m. No significant differences were recorded in 2008, while 2012 showed a decrease in size and ρ of the lens at $z = 50$ m all over the x axis. This process was even more evident in the measurements from 2019, where the ρ of the core dropped down to
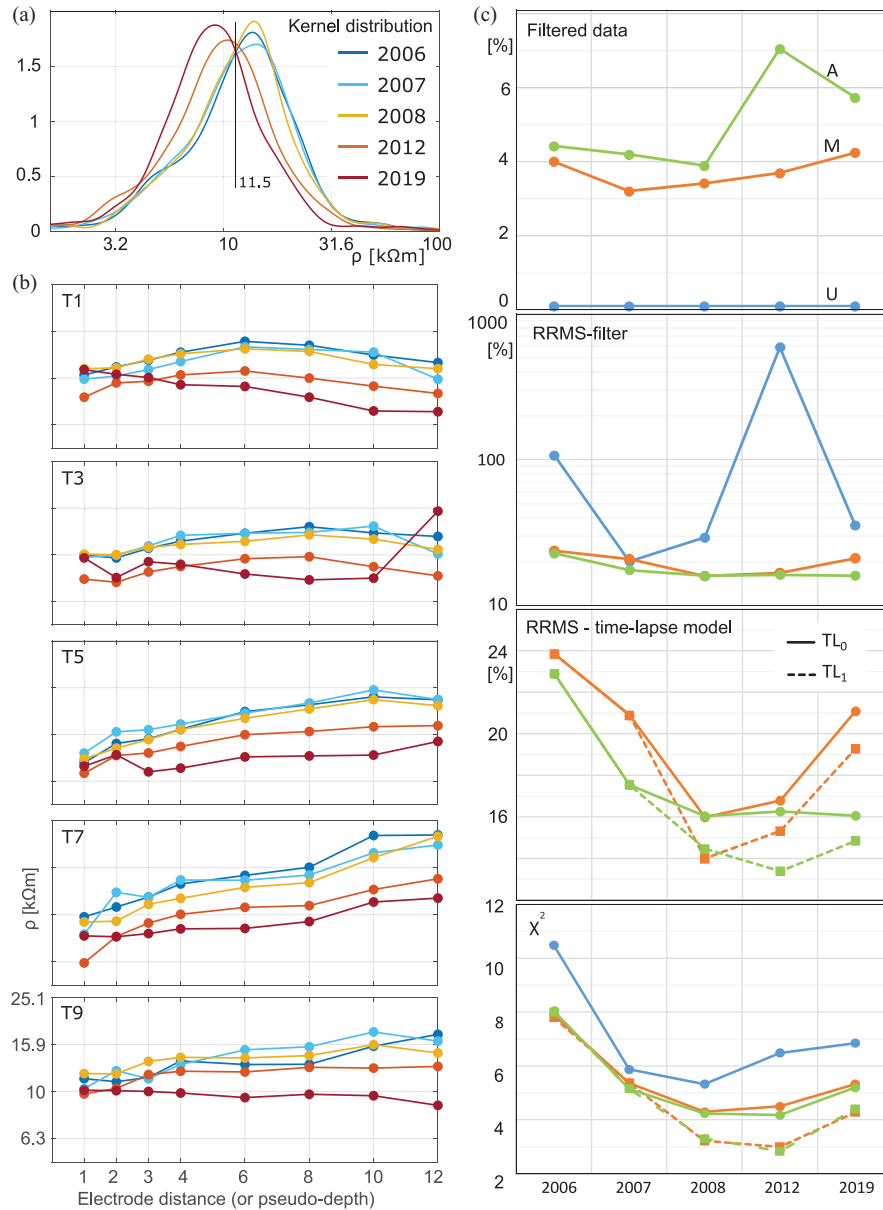
Figure 6 Left: changes in apparent resistivity of unfiltered data. (a) Comparison of probability density functions for all the transects, by year. (b) Comparison of average values at different pseudo-depth (PD), displayed separately for each ERT measurement transect. Right: Data fitting of inversions, in blue unfiltered data (U), in orange manually filtered data (M) and in green automatically filtered data (A). Continuous lines are obtained using always the first model as constrain (TL$_0$, dotted lines using at each step the previous model (TL$_1$). (c) From top to bottom: percentage of excluded data, RRMS with U/M/A, RRMS with different time-lapse mode and χ^2 with U/M/A and time-lapse models.

22.4 kΩm. At the toe of the NE slope, high resistivities were evident only at $x = 0$, 4 and 8 m, while $x = 12$–16 m showed signs of resistivity decrease. An exception was the very steep part of the rock wall at $x = 16$ m, $z = 50$ m, which maintained its high resistivities over time.

On the ridge, the NE side above $z = 50$ m presented ρ at the lower limit of the transitional range (11.2 kΩm) in

2006. The conditions were stable until 2008, but this value decreased significantly in 2012 and 2019. This resulted in a low ρ corridor (down to 5 kΩm) perpendicular to surface between $y = 155$–170, $z = 45$–55 m, which was well documented at $x = 4$ m and already evident but still forming in $x = 0$ and 8 m. The SW side of the summit presented two small but remarkable high-ρ surface bodies at 0/180/50 m ($x/y/z$) and

Table 3 (A) Raw data analysis: mean apparent resistivity values, obtained from the PDFs in Figure 5, with percentage differences to 2006 (Δ_{2006}). (B) Exemplary volume estimate for model with manual filter and time-lapse scheme 1 (M_1). (C) Volumetric analysis: average volume of permafrost, percentual changes compared with 2006, decrease rate of volume per year compared with previous measurement and average volume in the TR

	2006	2007	2008	2012	2019
A. Raw data analysis					
$\mu_{\rho a}$ (kΩm)	11.6	11.5	11.4	9.4	8.9
$\Delta_{2006}\,\mu_{\rho a}$ (%)	–	−1	−2	−20	−23
B. Estimated permafrost volumes for model M_1 (m^3)					
Maximum ($\rho > 11.5$ kΩm)	7430	6600	6340	5310	4260
Average ($\rho > 13.25$ kΩm)	6770	6070	5650	4740	3440
Minimum ($\rho > 15$ kΩm)	6130	5450	5020	4170	2800
C. Volumetric analysis					
Average PF volume (m^3)	6790	6150	5860	5050	3880
Δ_{2006} volume (%)	–	−9	−14	−26	−43
Δ volume/year (%/y)	–	−9.4	−4.7	−3.5	−3.3
Transition-range volume (m^3)	1290	1110	1100	1230	2010
	± 645	± 555	± 550	± 615	± 1005

4/173/55 m, which reached a depth of 5 m and connected with each other. These two bodies preserved their ρ values and were evident even in 2019, when the low-ρ corridor was well established. Similar effects can also be found lower on the SW slope (e.g., in $x = 12$–18 m at $y = 182 / z = 45$–48 m).

The lower part of the SW slope and its toe presented $\rho < 8$ kΩm at $x = 0$ m, $y = 190$–170 m and $z = 40$–50 m in 2006 with a light increase up to 10 kΩm in direction $x = 16$ m, where in fact half of this area was close to TR values. In 2007, the low-ρ area expanded almost to $y = 160$ m for $x = 0$–12 m and showed a sharp decrease of ρ down to 4 kΩm. While this trend continued until 2008, values in this area were not showing significant ρ changes in 2012 and 2019 but only increase in surface and volume.

In 2006, the central lower core of the ridge ($y = 170$–180 m, $z = 30$–45 m) showed a 10 m-wide area with values in the TR (11.5–15 kΩm). In the following years, the high resistant core moved towards the NE slope and got thinner down to 5 m or less, as it can be seen in 2007–2008 for all x sections. In 2012 the area was centred at $y = 160$ m, and it started to expand. Due to the significant ρ reduction of the high-ρ body on the NE slope in 2019, this area expanded exponentially and reached the surface of the slope with width up to 15 m at some points.

The examination of 2D slices perpendicular to measurements in Figure 8 allowed the detection of different dynamics. At $x = 155$ m (NE side of the crest), ρ decreased quite homo-geneously from the surface into the bedrock. In 2006, high ρ ($\rho > 15$ kΩm) started at $z = 55$ m, under an approximately 3 m-thick TR area and extended until $z = 30$ m. Small changes were recorded in 2007 and 2008, while in 2012 the beginning of high ρ shifted down to $z = 40$ m for $x = 0$–10 m and TR areas strongly increased. In 2019, ρ decreased also in $x = 10$–16 m with the beginning of high ρ moving further down to $z = 35$ m but with ρ decreasing even under that.

The southwest side of the crest ($x = 172$ m) presented a wider low resistivity 'couloir' ($\rho < 8$ kΩm) between two very-high-ρ surface bodies ($\rho > 40$ kΩm), which very likely revealed ice-filled and/or air-filled fractures. In 2006 the 'couloir' had low ρ between $z = 60$ m and 50 m and TR resistivities between $z = 50$ and 55 m. Subsequent time-lapse images showed an overall absolute increase of ρ in 2007 and 2008 and an expansion of the corridor on the x axis starting in 2012. In 2019, this structure reached a width of 10 m at $z = 55$ m and of 15 m at $z = 45$ m. Despite these changes, the two high-ρ surface bodies preserved their values and extension.

Estimated permafrost volumes

Changes in permafrost between 2006 and 2019 are presented graphically in Figure 9. Figure 9(a) shows permafrost extension between the two years, while Figure 9(b) shows ρ differences in the lost areas. Decreases in ρ of up to 60% were mostly located under the active layer; on the contrary, changes
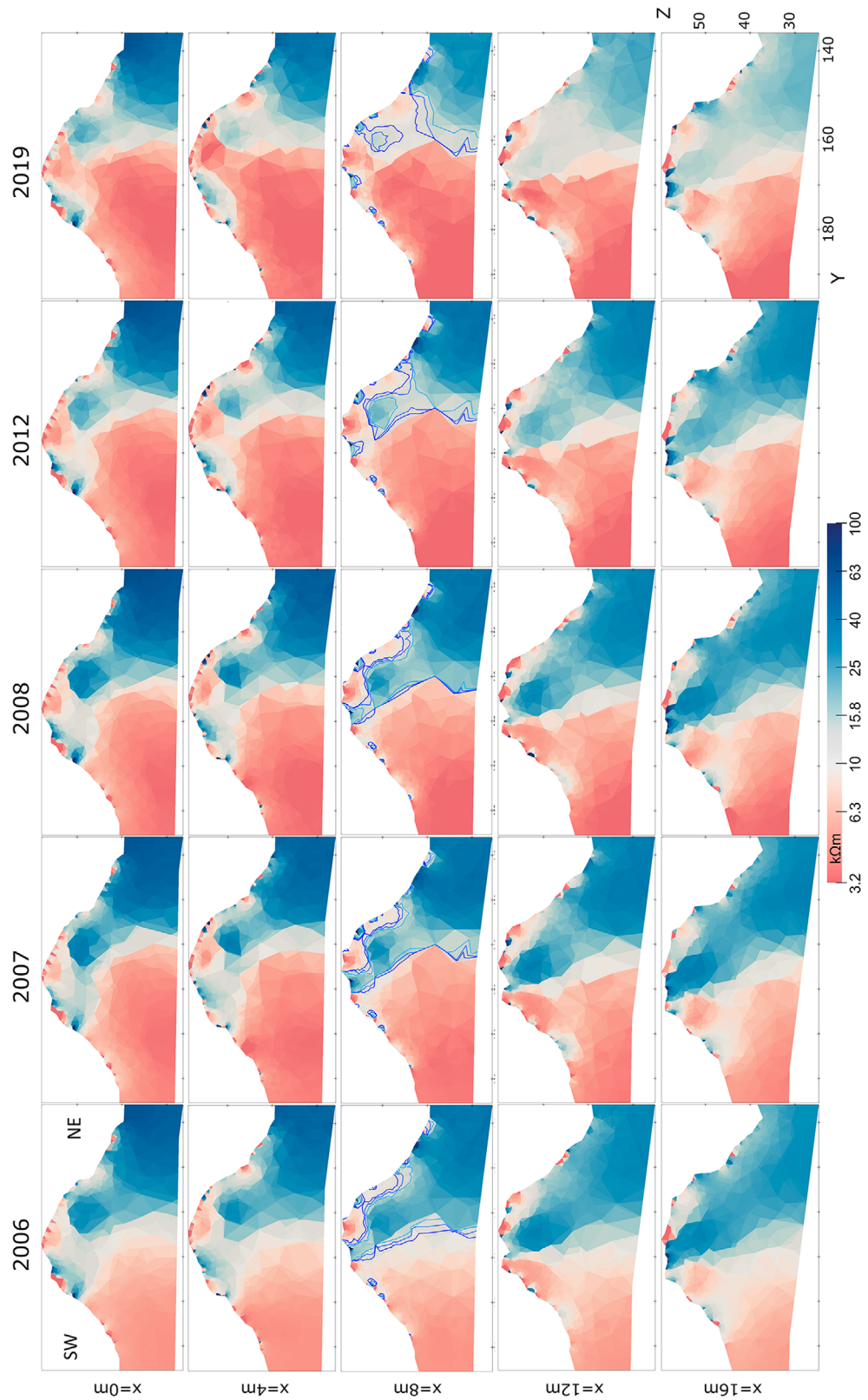
Figure 7 Results from the 3D inversion: vertical slices parallel to the direction of measurements, at the location of transects, $x = 0, 4, 8, 12$ and 16 m. Three isolines present in the graphs $x = 8$ m are representing minimum, mean and maximum values of the TR: 11.5, 13.25 and 15 kΩm, respectively. The extent of permafrost significantly decreases over time in all the transects.
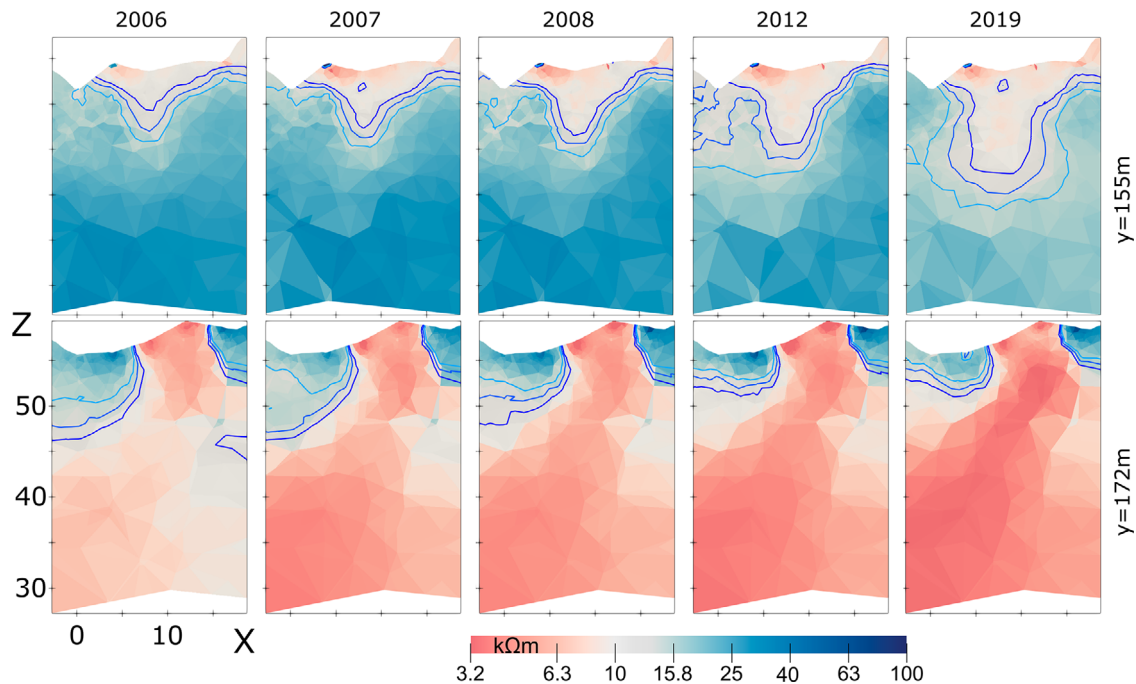
Figure 8 Vertical slices perpendicular to the direction of measurement at $y = 155$ m and 172 m. The isolines are representing minimum, average, and maximum value of the TR: 11.5, 13.25 and 15 kΩm, respectively.

in the active layer were mainly limited to between 0% and −30%. Figure 9(c and d) presents ρ changes according to three categories: (i) frozen, which includes values bigger than the TR, (ii) values in the TR and (iii) unfrozen, which includes values smaller than the TR. Here it is evident how the strongest changes—from frozen directly to unfrozen— happened at depth, in the core of the ridge. Some active layer in the north slope and part of the south slope were categorized as TR in 2006 and are now unfrozen. In 2006, most of the north slope under the active layer and some parts of the core were frozen but in 2019 they were in the TR.

Figure 10(a) shows, for the first time, a geophysically constrained quantitative volume estimation of bedrock permafrost and its degradation over the last 13 years. All models confirm a comparable decrease of volumes between 2006 and 2019. Unfiltered data showed the biggest volumes compared with automatic and manual filtered data. Marked differences were evident when changing the time-lapse model: constraining each model with the previous (TL$_1$) produced smaller permafrost volumes.

In an exemplary way, the reported volumes for the model M$_1$ in Table 3B and the average of all models in Table 3C. Here, all volumes should be understood as approximation and not as a precise measure; therefore, data are presented by rounding them to the closest tens. We calculated 6790 ±

645 m^3 of bedrock with $\rho > 13.25$ kΩm in 2006, which reduced to 3880 ± 1005 m^3 in 2019. We interpret this as a 43% volumetric decrease of frozen bedrock. These results, together with the mean resistivity and the five-year moving mean of MMAT, are also plotted in Figure 10(b). Here, it is possible to directly compare the inverse trends of temperature and resistivity/volumes. Strong changes in volumes (−9%) took place between 2006 and 2007, while resistivity dropped mainly between 2008 and 2012 (−20%). Air temperature showed a five-year moving mean decreasing until 2013 and then increasing dramatically in the last seven years. Permafrost volume, on the contrary, decreases steady also in the last period, with a light increase of the volumes classified in the TR. The volume included in the TR is rather stable (∼600 m^3) between 2006 and 2012, but increases to 1000 m^3 in 2019.

DISCUSSION

Applicability of laboratory-calibrated 4D electrical resistivity tomography in steep permafrost rock walls

It is not expected that geophysical methods can constrain permafrost distribution with extreme spatial accuracy, but they are probably up to date the best developed tool to estimate
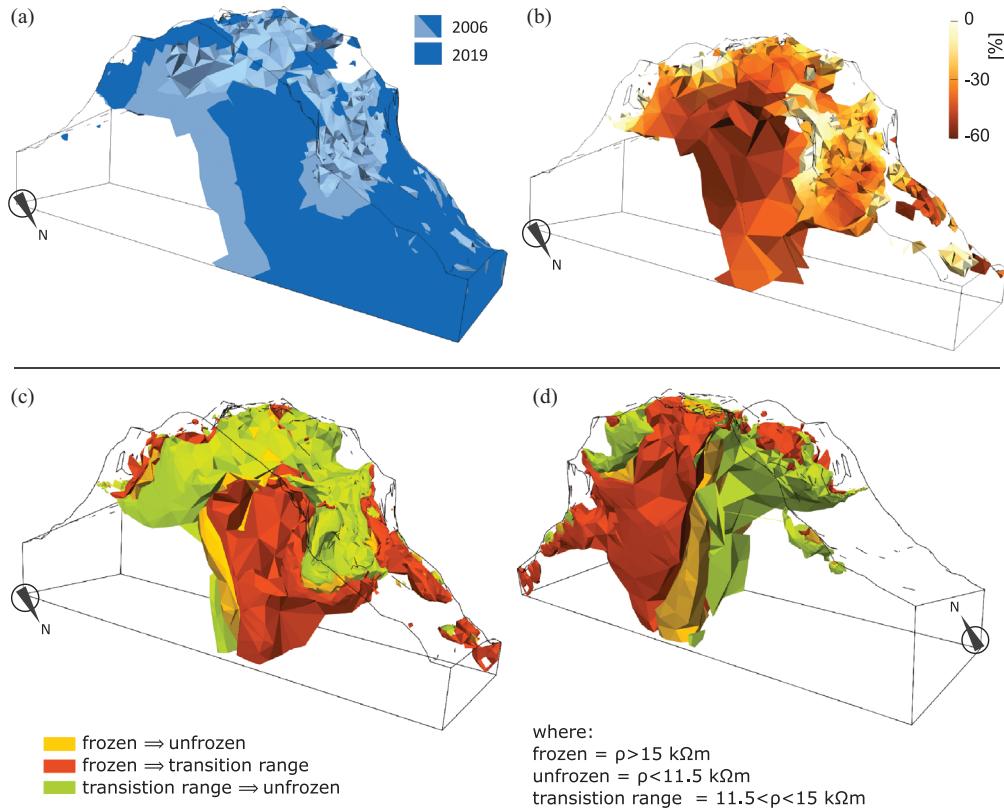
Figure 9 Changes in permafrost extension between 2006 and 2019. (a) Permafrost extensions obtained with $\rho > 13.25$ kΩm. (b) Difference of permafrost volumes between 2006 and 2019, corresponding therefore to the light blue volume in illustration (a). Colours indicate the decrease of resistivity. (c–d) Classification of changes in three categories, represented with smoothed surfaces with two opposite points of view. The parts of the model that were definitely frozen in 2006 and became definitely unfrozen in 2019 are here highlighted in yellow. In red are marked the parts that changed from definitely frozen to transition range, while in green those that were in the transition range and are now definitely unfrozen.

permafrost distribution and to monitor changes in frozen bedrock. As the freezing resistivity range of different lithologies varies significantly, laboratory calibration is essential. Only owing to the congruent calibration of multiple samples from the field site, we can interpret resistivity values $> 13.25 \pm 1.75$ kΩm as permafrost. Even if this range already includes uncertainties in the calibration due to supercooling effects (Krautblatter *et al*., 2010), resistivity values of intact laboratory samples might not exactly represent the fractured rock walls in the field. In fact, the degree of saturation, pore distribution and interconnectivity of pore throats as well as distribution and orientation of cracks and fractures influences electrical properties of rocks (Jouniaux *et al*., 2006; Zisser *et al*., 2007; Krautblatter *et al*., 2010). In this case, fractures are indeed supposed to be the cause of the extremely high resistivity values (> 100 kΩm) repeatedly measured on the surface, while rarely were located at depth, possibly due to more intact and homogeneous lithology.

True 3D measurements, i.e., employing measurements across acquisition lines, in periglacial environment have been successfully conducted by Draebing and Eichel (2017) on gentle moraine slopes and smaller landforms in a roll-along set-up (Doetsch *et al*., 2012); however, the size of the Steintaelli Ridge, the required pseudo-depth (PD) and the complexity of its topography with steep walls made a similar approach not feasible. Instead, data have been collected in quasi-3D using multiple parallel 2D transects. According to Chambers *et al*. (2002), excluding perpendicular transects could lead to accentuate perpendicular structures in 3D imaging. Since our main high-resistivity body is located under the NE slope, exactly perpendicular to measurement direction, we cannot exclude an overestimation of its extension, which would result in an overestimation of permafrost volumes. As this effect is constant over the years, we do not expect a strong influence on the overall degradation rate of permafrost given by the difference between subsequent time sections. Rödder and Kneisel (2012)
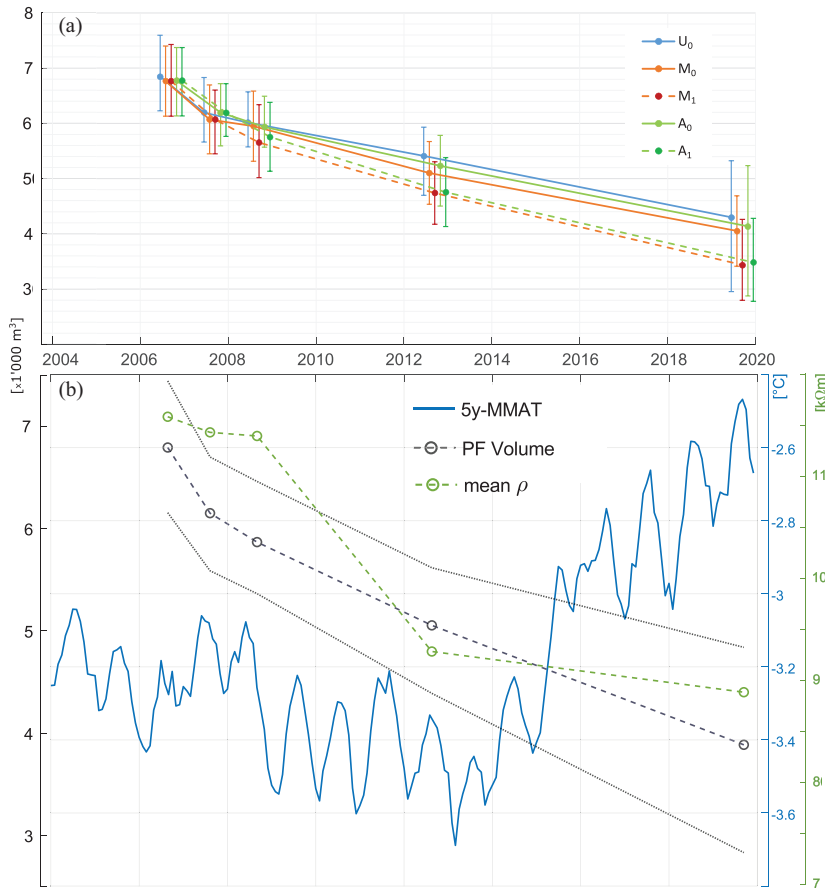
Figure 10 (a) Volumetric estimation of permafrost: points are representing the volume of all the cells with $\rho>13.25$ kΩm, while the lower (upper) error bars represent the volume of cells with $\rho > 11.5$ kΩm ($\rho > 15$ kΩm). (b) The average permafrost volume of all the models is here represented with a dashed grey line, with confidence intervals as pointed lines. In blue is shown the moving mean of the mean monthly air temperature, with period five years before date, and in green the average apparent resistivity of the raw data.

showed for periglacial environments that using only parallel 2D transect instead of combining parallel and perpendicular transects delivers very similar results. This is especially true when the distance between the parallel transects is, like in our case, only two times the transect internal electrode distance.

The analysis of raw data using probability density functions (Fig. 6a) presents a gradual reduction of the mean ρ_a from 2006 to 2019, explained by a decrease of probability density for $\rho_a > 11.5$ kΩm and a consequent increase for < 11.5 kΩm. Similarly, the results of the PD analysis reveal that for PD > 4, mean ρ_a reached values < 11.5 kΩm everywhere in 2019. The outlier in transect 3 (Fig. 6b) at PD = 12 in 2019 is biased by a single measurement error, since we show here unfiltered data. The value of 11.5 kΩm occurs to be the lowest border of the transition range (TR) obtained from laboratory calibration, suggesting that major phase changes happened inside the rock mass. Figure 6(a, b) demonstrates that the decrease in resistivity is present even prior to filtering and not an inversion artefact. This assumption strongly supports our results, and it is fundamental for the following

volumetric analysis. We are aware of the fact that shallower measurements affect the deeper ones; nevertheless, Figure 9(a) demonstrates that only minor resistivity changes happened at shallow layers compared with deeper layers. Therefore, we hypothesize that resistivity changes at depth have a bigger magnitude than the effects given by superficial layers.

An accurate selection of outliers previous to inverse modelling is crucial, and the exclusion of just a few data points from the calculations can strongly improve relative root mean square (RRMS; Fig. 6c). During manual filtering, we noticed that some outliers approach identical values in subsequent annual measurements. As Lysdahl *et al.* (2017) shows, the comparison of repeated independent measurements can help to distinguish real features from measurement errors. Figure 7 shows values close to or above 100 kΩm on the surface of more neighbouring transects in every year. These values would theoretically correspond to rock temperatures below −10°C, highly improbable as rock surface temperatures during summer (Draebing *et al.*, 2017) and borehole measurements in Switzerland at similar sites recorded rock temperatures in a

range between −2°C and −3°C at 20 m depth (Noetzli, Pellet and Staub, 2019). According to laboratory measurements, these values rather indicate ice intercalations (e.g., segregation ice) or massive ice in crevices when reaching 1 MΩm. Both these phenomena have been detected on this site and documented by crackmeters (Draebing, Krautblatter and Hoffmann, 2017) and pseudo-3D seismic refraction tomography (Krautblatter and Draebing, 2014; Draebing et al., 2017).

Automatic filtering is quick and delivers better visual results (tomograms not shown here) as well as better data fitting (RRMS, χ^2) compared with unfiltered data, although leading to the exclusion of a few values that could represent real features, as just shown in the previous paragraph. Manual filtering is more time intensive, but provides the best results in data fitting and allows to include real features and to decipher measurements errors. Other filtering approaches, such as the use of reciprocal or short-term repeated measurements and their error estimates, could possibly improve inversion results, but require increased time and power, both precious resources in high alpine terrain. On the contrary, using stacking errors may lead to underestimation of uncertainties (Tso et al., 2017). *Side-view pseudosections* provide an additional tool to select the minimum and maximum limits for automatic filtering as well as to detect outliers for manual filtering, thanks to their 3D visualization of raw data. We recommend laboratory calibration of samples to support filtering and data interpretation, since it is the only method that can provide a $T–\rho$ relationship under controlled conditions.

The resulting values of RRMS are similar to other examples in BERT (Martin and Günther, 2013; Lysdahl et al., 2017). The chi-squared misfit shows reliable results without overfitting or underfitting the data when $\chi^2 < 5$ (Günther, Rücker and Spitzer, 2006), which we obtain in all simulations apart from 2006. Tests with further inversion settings have been conducted but are not shown here for place limitations and redundancy of results. In fact, in all the other inversions, values of RRMS and χ^2 were changing but volumes remained within the confidence interval shown here. Models computed with TL_1 deliver better results than with TL_0. Raw data analysis, inversion performance and plausibility checks indicate that laboratory-calibrated quasi-3D electrical resistivity tomography (ERT) can provide a robust monitoring tool for permafrost monitoring.

Permafrost evolution in the Steintaelli

Long-term air temperature trends at the Steintaelli show an increase of ∼0.8°C between 2005–2009 and 2015–2019,

with rates significantly growing in the second period. Climate change studies in the Alpine region quantified a 2.0°C ± 0.6°C mean annual air temperature increase above 3000 m between 1900 and 2004 (Gilbert and Vincent, 2013), with four times higher rates in 1970−2009 than in 1934–1970 (Mourey et al., 2019). Further records indicate that the period 2014–2018 is the warmest ever recorded in Switzerland since measurements began in 1864 (Noetzli, Pellet and Staub, 2019), in agreement with our data and very likely leading to permafrost degradation.

Between the known monitoring studies in the Alps (Krautblatter et al., 2010; Supper et al., 2014; Keuschnig et al., 2017; Mollaret et al., 2019; Noetzli, Pellet and Staub, 2019), numerical quantification of resistivity changes seems very rare. Hilbich et al. (2008) showed maximal inter-annual resistivity changes up to 35% between 1999 and the hot summer of 2003, while Mollaret et al. (2019) reported a 'distinct' reduction in average resistivity between 2009 and 2013 at five sites simultaneously. Looking at results in Figure 10, we can see changes in mean resistivity of raw data up to −23% from 2006 to 2019, that we interpreted as increase of rock temperatures and a respective decrease in the proportion of permanently frozen rock in the rock mass.

The presented 3D inversions go beyond the standard 2D analysis of permafrost changes and allow volumetric evaluation of changes (Fig. 9). Due to laboratory calibration of the bedrock at the study site, we are able to estimate the frozen and unfrozen parts of the ridge. By this, we can compute the total volume of frozen bedrock for the first time and its reduction in time. Permafrost volume reduces of 43% in 13 years.

Our data show corridors with lower resistivity within high resistive bodies, which potentially indicate preferred paths for heat fluxes due to hydraulic conductivity along fractures (Krautblatter, 2010).

Volumetric permafrost degradation occurs gradually with similar rates over the monitoring period (Table 3); however, the degradation rate is not always directly connected to an increase of air temperatures. Between 2006 and 2015, alternating warmer and colder than average years were recorded by the meteorological station; however, the volumetric calculation of permafrost suggests a decrease in the same period. The warming phase that started in 2013 (Noetzli, Pellet and Staub, 2019 and Fig. 4) apparently did not accelerate permafrost degradation as indicated by mean permafrost volume and degradation rate (see, Table 3). The influence of air temperature changes on permafrost is reduced by insulating snow cover (Draebing et al., 2017) and, therefore, air temperature changes only affect near-surface part of the active layer

(Krautblatter and Draebing, 2014; Draebing *et al.*, 2017). Our data suggest a delayed response of permafrost to a long-term air temperature trend. According to climate scenarios (Gobiet *et al.*, 2014), air temperature will increase with a trend of 0.25°C to 0.35°C per decade and permafrost will respond delayed to this warming trend. Knowing that the rock mass in *phase transition* increased 70% in the last seven years, we expect not only permafrost degradation to continue, but also degradation rates to increase. These can also be increased by heat transport along fracture by percolating water, which can rapidly increase the thermal regime (Draebing *et al.*, 2014; Phillips *et al.*, 2016).

Implications of permafrost warming and degradation on rock wall stability

Rock slope failures vary from m³ size rockfall (Kenner *et al.*, 2011; Ravanel *et al.*, 2013; Hartmeyer *et al.*, 2020) to rock avalanches of millions of m³ (Sosio *et al.*, 2008; Walter *et al.*, 2020). Studies over the last century demonstrated an increase in rockfall activity from permafrost-affected walls between 1990 and 2009 (Ravanel and Deline, 2010), with a strong correlation between rockfalls and the warmest summers (e.g., 2003, 2015) when the number of rockfalls increased three to four times compared with average summers (Ravanel *et al.*, 2017). They suggest a contribution of permafrost degradation by long-term climate change, amplified by heat waves. Our observed data demonstrate a permafrost degradation and an increase of masses close to thawing point.

Permafrost warming and thawing reduce the shear resistance by increasing the creep and fracture of ice within fractures and the fracture of rock–ice contacts, the friction along rock–rock contacts and the fracture of intact rock bridges (Krautblatter, Funk and Günzel, 2013). Concerning the first point, multiple mechanical factors influencing rock stability like fracture toughness, compressive and tensile strength are sensitive to temperature changes and can decrease by up to 50% when intact water-saturated rock thaws (Mellor, 1973; Krautblatter, Funk and Günzel, 2013). The factor of safety of slopes will also reduce when temperature rises if a slope presents ice-filled joints, since stiffness and strength of an ice-filled joint are a function of both normal stress and temperature (Davies *et al.*, 2001). Regarding the second point, more unfrozen material means more material exposed to cryo- and hydrostatic pressures, which are both well-known destabilizing factors (Sosio, Crosta and Hungr, 2008; Fischer *et al.*, 2010; Phillips *et al.*, 2017). As a result, an increase in the frequency and size of destabilizing events can be postulated.

Therefore, our data suggest that the stability of the Steintaelli Ridge decreases with time.

Rock wall instability in permafrost rocks is threatening infrastructures and people not only in the high alpine summits, but also in the valleys downstream, due to possible uncontrolled subsequent cascading effects (Walter *et al.*, 2020). The understanding of processes that dispose, detach and trigger rockfalls is fundamental and strictly connected to the internal thermal state of bedrock. While the drilling of boreholes has important cost, difficult logistics and provides only 1D results, geophysical sounding comes at much lower human and economical effort and can provide 3D spatial information on permafrost presence and development, a crucial information for evaluating slope stability. Monitoring with 4D ERT provides a new tool for the spatial and temporal analysis of rock permafrost degradation, which is strictly connected with active rock deformations and sliding processes, preparatory components of rockslides.

CONCLUSIONS

We conducted a high-resolution pseudo-3D electrical resistivity measurements along five parallel transects across the permafrost-affected Steintaelli Ridge at 3150 m a.s.l. in the Matter Valley (CH) in summer 2006, 2007, 2008, 2012 and 2019 with virtually identical set-up and measurement devices. A 4D data inversion was performed using the software BERT with a tetrahedral mesh composed of about 20,000 nodes, robust data reweighting and time-lapse scheme. Bedrock temperatures have been linked to resistivity thanks to T–ρ laboratory calibration of two samples from the ridge. Calibration of Matter Valley quartz schist results in a bilinear T–ρ relationship with phase transition by 13.25 ± 1.75 kΩm. According to this range, estimation of frozen volumes has been conducted and changes in the 13 years of monitoring were assessed.

Air temperature in the region shows alternating warmer and colder years between 2006 and 2015 and a very steep increase in the last five years. However, the volume of frozen bedrock decreases regularly from 6790 ± 640 m³ in 2006 to 3880 ± 1000 m³ in 2019, implying a volumetric loss of 43% of permafrost in total. Raw data analysis, the application of filter techniques and time-lapse models confirm the robustness of the obtained volumes. The observed increase of unfrozen masses in steep rock walls will further be amplified by climate change, and it is likely to lead to an increase in size and frequency of instability phenomena like creeping, rockfalls and slides, which are threatening structures and people in high alpine environments as well as in the downstream valleys.

Calibrated 4D electrical resistivity tomography has proven to be a robust method to detect, monitor and conceivably predict these hazards.

CONTRIBUTION

Field set-up, sample calibration and fieldwork in 2006, 2007 and 2008 were conducted by MK. Fieldwork in 2012 was conducted by DD. Fieldwork in 2019 was conducted by RS, climate data analysis and 2D/3D inversion were conducted by RS and MO. Text was redacted by RS and reviewed by DD, MO and MK.

DATA AVAILABILITY STATEMENT

The data that support the findings of this study are available from the corresponding author upon reasonable request.

ORCID

Riccardo Scandroglio
https://orcid.org/0000-0002-5434-8382
Daniel Draebing https://orcid.org/0000-0001-6379-4707
Michael Krautblatter
https://orcid.org/0000-0002-2775-2742

REFERENCES

Biskaborn, B.K., Smith, S.L, Noetzli, J., Matthes, H., Vieira, G., Streletskiy, D.A, *et al*. (2019) Permafrost is warming at a global scale. *Nature Communications*, 10(1), 264. https://doi.org/10.1038/s41467-018-08240-4.

Boeckli, L., Brenning, A., Gruber, S. and Noetzli, J. (2012) Permafrost distribution in the European Alps: calculation and evaluation of an index map and summary statistics. *Cryosphere*, 6(4), 807–820. https://doi.org/10.5194/tc-6-807-2012.

Casty, C., Wanner, H., Luterbacher, J., Esper, J. and Böhm, R. (2005) Temperature and precipitation variability in the European Alps since 1500. *International Journal of Climatology*, 25(14), 1855–1880. https://doi.org/10.1002/joc.1216.

Chambers, J.E., Ogilvy, R.D., Kuras, O., Cripps, J.C. and Meldrum, P.I. (2002) 3D electrical imaging of known targets at a controlled environmental test site. *Environmental Geology*, 41(6), 690–704. https://doi.org/10.1007/s00254-001-0452-4.

Davies, M.C.R., Hamza, O. and Harris, C. (2001) The effect of rise in mean annual temperature on the stability of rock slopes containing ice-filled discontinuities. *Permafrost and Periglacial Processes*, 12(1), 137–144. https://doi.org/10.1002/ppp.378.

Doetsch, J., Linde, N., Pessognelli, M., Green, A.G. and Günther, T. (2012) Constraining 3-D electrical resistance tomography with GPR reflection data for improved aquifer characterization. *Journal of Applied Geophysics*, 78, 68–76. https://doi.org/10.1016/j.jappgeo.2011.04.008.

Draebing, D. and Eichel, J. (2017) Spatial controls of turf-banked solifluction lobes and their role for paraglacial adjustment in glacier forelands. *Permafrost and Periglacial Processes*, 28(2), 446–459. https://doi.org/10.1002/ppp.1930.

Draebing, D., Haberkorn, A., Krautblatter, M., Kenner, R. and Phillips, M. (2017) Thermal and mechanical responses resulting from spatial and temporal snow cover variability in permafrost rock slopes, Steintaelli, Swiss Alps. *Permafrost and Periglacial Processes*, 28(1), 140–157. https://doi.org/10.1002/ppp.1921.

Draebing, D. and Krautblatter, M. (2012) P-wave velocity changes in freezing hard low-porosity rocks: a laboratory-based time-average model. *The Cryosphere*, 6(5), 1163–1174. https://doi.org/10.5194/tc-6-1163-2012.

Draebing, D., Krautblatter, M. and Dikau, R. (2014) Interaction of thermal and mechanical processes in steep permafrost rock walls: a conceptual approach. *Geomorphology*, 226(November), 226–235. https://doi.org/10.1016/j.geomorph.2014.08.009.

Draebing, D., Krautblatter, M. and Hoffmann, T. (2017) Thermo-cryogenic controls of fracture kinematics in permafrost rockwalls, *Geophys. Res. Lett*., 44(8), 3535–3544, https://doi.org/10.1002/2016GL072050.

Duvillard, P.A., Revil, A., Qi, Y., Soueid Ahmed, A., Coperey, A. and Ravanel, L. (2018) Three-dimensional electrical conductivity and induced polarization tomography of a rock glacier. *Journal of Geophysical Research: Solid Earth*, 123(11), 9528–9554. https://doi.org/10.1029/2018JB015965.

Emmert, A. and Kneisel, C. (2017) Internal structure of two alpine rock glaciers investigated by quasi-3-D electrical resistivity imaging. *Cryosphere*, 11(2), 841–855. https://doi.org/10.5194/tc-11-841-2017.

Fischer, L., Amann, F., Moore, J.R. and Huggel, C. (2010) Assessment of periglacial slope stability for the 1988 Tschierva rock avalanche (Piz Morteratsch, Switzerland). *Engineering Geology*, 116(1–2), 32–43. https://doi.org/10.1016/j.enggeo.2010.07.005.

Gharibi, M. and Bentley, L.R. (2005) Resolution of 3-D electrical resistivity images from inversions of 2-D orthogonal lines. *Journal of Environmental and Engineering Geophysics*, 10(4), 339–349. https://doi.org/10.2113/JEEG10.4.339.

Gilbert, A. and Vincent, C. (2013) Atmospheric temperature changes over the 20th century at very high elevations in the European Alps

from englacial temperatures. *Geophysical Research Letters*, 40(10), 2102–2108. https://doi.org/10.1002/grl.50401.

Gobiet, A., Kotlarski, S., Beniston, M., Heinrich, G., Rajczak, J. and Stoffel, M. (2014) 21st century climate change in the European Alps – a review. *Science of the Total Environment*, 493, 1138–1151. https://doi.org/10.1016/j.scitotenv.2013.07.050.

Gruber, S. and Haeberli, W. (2007) Permafrost in steep bedrock slopes and its temperature-related destabilization following climate change. *Journal of Geophysical Research*, 112(F2), F02S18. https://doi.org/10.1029/2006JF000547.

Gruber, S. and Hoelzle, M. (2001) Statistical modelling of mountain permafrost distribution: local calibration and incorporation of remotely sensed data. *Permafrost and Periglacial Processes*, 12(1), 69–77. https://doi.org/10.1002/ppp.374.

Gruber, S., Hoelzle, M. and Haeberli, W. (2004) Permafrost thaw and destabilization of Alpine rock walls in the hot summer of 2003. *Geophysical Research Letters*, 31(13), L13504. https://doi.org/10.1029/2004GL020051.

Günther, T. and Rücker, C. (2019) Manual, Boundless electrical resistivity tomography BERT: The user tutorial.

Günther, T., Rücker, C. and Spitzer, K. (2006) Three-dimensional modelling and inversion of dc resistivity data incorporating topography – II. Inversion. *Geophysical Journal International*, 166(2), 506–517. https://doi.org/10.1111/j.1365-246X.2006.03011.x.

Harris, C., Mühll, D.V., Isaksen, K., Haeberli, W., Sollid, J.L., King, L., *et al*. (2003) Warming permafrost in European mountains. *Global and Planetary Change*, 39(3–4), 215–225. https://doi.org/10.1016/j.gloplacha.2003.04.001.

Hartmeyer, I., Delleske, R., Keuschnig, M., Krautblatter, M., Lang, A., Otto, J.C., *et al*. (2020) Current glacier recession causes significant rockfall increase : The immediate paraglacial response of deglaciating cirque walls. *Earth Surf. Dynam*, 8(March), 1–25. https://doi.org/10.5194/esurf-8-729-2020.

Hauck, C. and Mühll, D.V. (2003) Inversion and interpretation of two-dimensional geoelectrical measurements for detecting permafrost in mountainous regions. *Permafrost and Periglacial Processes*, 14(4), 305–318. https://doi.org/10.1002/ppp.462.

Hilbich, C., Hauck, C., Hoelzle, M., Scherler, M., Schudel, L., Völksch, I., *et al*. (2008) Monitoring mountain permafrost evolution using electrical resistivity tomography: a 7-year study of seasonal, annual, and long-term variations at Schilthorn, Swiss Alps. *Journal of Geophysical Research*, 113(F1), F01S90. https://doi.org/10.1029/2007JF000799.

Hock, R., Rasul, G., Adler, C., Cáceres, B., Gruber, S., Hirabayashi, Y., *et al*. (2019) Chapter 2: High mountain areas. IPCC Special Report on the Ocean and Cryosphere in a Changing Climate. *IPCC Special Report on the Ocean and Cryosphere in a Changing Climate*, 131–202.

Huggel, C. (2009) Recent extreme slope failures in glacial environments: effects of thermal perturbation. *Quaternary Science Reviews*, 28(11–12), 1119–1130. https://doi.org/10.1016/j.quascirev.2008.06.007.

IPCC (2014) *Climate change 2014: Synthesis report. Contribution of working groups I, II and III to the Fifth Assessment Report of the Intergovernmental Panel on Climate Change*. Core Writing Team, R. K. Pachauri, and L. A. Meyer (Eds.). Geneva, Switzerland: IPCC.

Jouniaux, L., Zamora, M. and Reuschlé, T. (2006) Electrical conductivity evolution of non-saturated carbonate rocks during deformation up to failure. *Geophysical Journal International*, 167(2), 1017–1026. https://doi.org/10.1111/j.1365-246X.2006.03136.x.

Kenner, R., Noetzli, J., Hoelzle, M., Raetzo, H. and Phillips, M. (2019) Distinguishing ice-rich and ice-poor permafrost to map ground temperatures and ground ice occurrence in the Swiss Alps. *The Cryosphere*, 13(7), 1925–1941. https://doi.org/10.5194/tc-13-1925-2019.

Kenner, R., Phillips, M., Danioth, C., Denier, C., Thee, P. and Zgraggen, A. (2011) Investigation of rock and ice loss in a recently deglaciated mountain rock wall using terrestrial laser scanning: Gemsstock, Swiss Alps. *Cold Regions Science and Technology*, 67(3), 157–164. https://doi.org/10.1016/j.coldregions.2011.04.006.

Keuschnig, M., Krautblatter, M., Hartmeyer, I., Fuss, C. and Schrott, L. (2017) Automated electrical resistivity tomography testing for early warning in unstable permafrost rock walls around alpine infrastructure. *Permafrost and Periglacial Processes*, 28(1), 158–171. https://doi.org/10.1002/ppp.1916.

Kneisel, C., Emmert, A. and Kästl, J. (2014) Application of 3D electrical resistivity imaging for mapping frozen ground conditions exemplified by three case studies. *Geomorphology*, 210, 71–82. https://doi.org/10.1016/j.geomorph.2013.12.022.

Krautblatter, M. (2009) *Detection and quantification of permafrost change in alpine rock walls and implications for rock instability*. Ph.D. Thesis. Friedrich-Wilhelms University Bonn.

Krautblatter, M. (2010) Patterns of multiannual aggradation of permafrost in rock walls with and without hydraulic interconnectivity (Steintälli, Valley of Zermatt, Swiss Alps). In Otto, J.-C. and Dikau, R. ((Eds.) Landform – Structure, Evolution, Process Control. Lecture Notes in Earth Sciences, *vol 115*. Berlin, Heidelberg: Springer, pp. 199–219. https://doi.org/10.1007/978-3-540-75761-0_13.

Krautblatter, M. and Draebing, D. (2014) Pseudo 3-D P wave refraction seismic monitoring of permafrost in steep unstable bedrock. *Journal of Geophysical Research: Earth Surface*, 119(2), 287–299. https://doi.org/10.1002/2012JF002638.

Krautblatter, M., Funk, D. and Günzel, F.K. (2013) Why permafrost rocks become unstable: a rock-ice-mechanical model in time and space. *Earth Surface Processes and Landforms*, 38(8), 876–887. https://doi.org/10.1002/esp.3374.

Krautblatter, M. and Hauck, C. (2007) Electrical resistivity tomography monitoring of permafrost in solid rock walls. *Journal of Geophysical Research: Earth Surface*, 112(2), 1–14. https://doi.org/10.1029/2006JF000546.

Krautblatter, M., Verleysdonk, S., Flores-Orozco, A. and Kemna, A. (2010) Temperature-calibrated imaging of seasonal changes in permafrost rock walls by quantitative electrical resistivity tomography (Zugspitze, German/Austrian Alps). *Journal of Geophysical Research: Earth Surface*, 115(2), 1–15. https://doi.org/10.1029/2008JF001209.

Lysdahl, A.K., Bazin, S., Christensen, C., Ahrens, S., Günther, T. and Pfaffhuber, A.A. (2017) Comparison between 2D and 3D ERT inversion for engineering site investigations – a case study from Oslo Harbour. *Near Surface Geophysics*, 15(2), 201–209. https://doi.org/10.3997/1873-0604.2016052.

Magnin, F., Krautblatter, M., Deline, P., Ravanel, L., Malet, E. and Bevington, A. (2015) Determination of warm, sensitive permafrost areas in near-vertical rockwalls and evaluation of distributed models by electrical resistivity tomography. *Journal of Geophysical Research: Earth Surface*, 745–762. https://doi.org/10.1002/2014JF003351.Received.

Mamot, P., Weber, S., Schröder, T. and Krautblatter, M. (2018) A temperature- and stress-controlled failure criterion for ice-filled permafrost rock joints. *The Cryosphere*, 12(10), 3333–3353. https://doi.org/10.5194/tc-12-3333-2018.

Martin, T. and Günther, T. (2013) Complex resistivity tomography (CRT) for fungus detection on standing oak trees. *European Journal of Forest Research*, 132(5–6), 765–776. https://doi.org/10.1007/s10342-013-0711-4.

Mellor, M. (1973) Mechanical Properties of Rocks at Low Temperatures, in *2nd Int. Conference on Permafrost*. Yakutsk, Russia, 334–344.

Mollaret, C., Hilbich, C., Pellet, C., Flores-Orozco, A., Delaloye, R. and Hauck, C. (2019) Mountain permafrost degradation documented through a network of permanent electrical resistivity tomography sites. *Cryosphere*, 13(10), 2557–2578. https://doi.org/10.5194/tc-13-2557-2019.

Mourey, J., Marcuzzi, M., Ravanel, L. and Pallandre, F. (2019) Effects of climate change on high Alpine mountain environments: evolution of mountaineering routes in the Mont Blanc massif (Western Alps) over half a century. *Arctic, Antarctic, and Alpine Research*, 51(1), 176–189. https://doi.org/10.1080/15230430.2019.1612216.

Murton, J.B., Kuras, O., Krautblatter, M., Cane, T., Tschofen, D., Uhlemann, S., *et al*. (2016) Monitoring rock freezing and thawing by novel geoelectrical and acoustic techniques. *Journal of Geophysical Research: Earth Surface*, 121(12), 2309–2332. https://doi.org/10.1002/2016JF003948.

Murton, J.B., Peterson, R. and Ozouf, J.-C. (2006) Bedrock fracture by ice segregation in cold regions. *Science*, 314(5802), 1127–1129. https://doi.org/10.1126/science.1132127.

PERMOS (2019) Permafrost in Switzerland 2014/2015 to 2017/2018, Noetzli, J., Pellet, C. and Staub, B. (Eds.). *Glaciological Report Permafrost No. 16–19 of the Cryospheric Commission of the Swiss Academy of Sciences*. pp. 104. https://doi.org/10.13093/permos-rep-2019-16-19.

Phillips, M., Haberkorn, A., Draebing, D., Krautblatter, M., Rhyner, H. and Kenner, R. (2016) Seasonally intermittent water flow through deep fractures in an Alpine Rock Ridge: Gemsstock, Central Swiss Alps. *Cold Regions Science and Technology*, 125, 117–127. https://doi.org/10.1016/j.coldregions.2016.02.010.

Phillips, M., Wolter, A., Lüthi, R., Amann, F., Kenner, R. and Bühler, Y. (2017) Rock slope failure in a recently deglaciated permafrost rock wall at Piz Kesch (Eastern Swiss Alps), February 2014. *Earth Surface Processes and Landforms*, 42(3), 426–438. https://doi.org/10.1002/esp.3992.

Pirulli, M. (2009) The Thurwieser rock avalanche (Italian Alps): description and dynamic analysis. *Engineering Geology*, 109(1–2), 80–92. https://doi.org/10.1016/j.enggeo.2008.10.007.

Pogliotti, P., Guglielmin, M., Cremonese, E., Morra Di Cella, U., Filippa, G., Pellet, C., *et al*. (2015) Warming permafrost and active layer variability at Cime Bianche, Western European Alps. *Cryosphere*, 9(2), 647–661. https://doi.org/10.5194/tc-9-647-2015.

Ravanel, L., Deline, P., Lambiel, C. and Vincent, C. (2013) Instability of a high alpine rock ridge: the Lower Arête Des Cosmiques, Mont Blanc Massif, France. *Geografiska Annaler, Series A: Physical Geography*, 95(1), 51–66. https://doi.org/10.1111/geoa.12000.

Ravanel, L. and Deline, P. (2010) Climate influence on rockfalls in high-Alpine steep rockwalls: The north side of the Aiguilles de Chamonix (Mont Blanc massif) since the end of the "Little Ice Age." *The Holocene*, 21(2), 357–365. https://doi.org/10.1177/0959683610374887.

Ravanel, L., Magnin, F. and Deline, P. (2017) Impacts of the 2003 and 2015 summer heatwaves on permafrost-affected rock-walls in the Mont Blanc massif. *Science of the Total Environment*, 609, 132–143. https://doi.org/10.1016/j.scitotenv.2017.07.055.

Rödder, T. and Kneisel, C. (2012) Permafrost mapping using quasi-3D resistivity imaging, Murtèl, Swiss Alps. *Near Surface Geophysics*, 10(2), 117–127. https://doi.org/10.3997/1873-0604.2011029.

Scherrer, S.C., Appenzeller, C., Liniger, M.A. and Schär, C. (2005) European temperature distribution changes in observations and climate change scenarios. *Geophysical Research Letters*, 32(19), 1–5. https://doi.org/10.1029/2005GL024108.

Siewert, M.B., Krautblatter, M., Christiansen, H.H. and Eckerstorfer, M. (2012) Arctic rockwall retreat rates estimated using laboratory-calibrated ERT measurements of talus cones in Longyeardalen, Svalbard. *Earth Surface Processes and Landforms*, 37(14), 1542–1555. https://doi.org/10.1002/esp.3297.

Sosio, R., Crosta, G.B. and Hungr, O. (2008) Complete dynamic modeling calibration for the Thurwieser rock avalanche (Italian Central Alps). *Engineering Geology*, 100(1–2), 11–26. https://doi.org/10.1016/j.enggeo.2008.02.012.

Supper, R., Ottowitz, D., Jochum, B., Römer, A., Pfeiler, S., Kauer, S., *et al*. (2014) Geoelectrical monitoring of frozen ground and permafrost in alpine areas: field studies and considerations towards an improved measuring technology. *Near Surface Geophysics*, 12(1), 93–115. https://doi.org/10.3997/1873-0604.2013057.

Tso, C.H.M., Kuras, O., Wilkinson, P.B., Uhlemann, S., Chambers, J.E., Meldrum, P.I., *et al*. (2017) Improved characterisation and modelling of measurement errors in electrical resistivity tomography (ERT) surveys. *Journal of Applied Geophysics*, 146, 103–119. https://doi.org/10.1016/j.jappgeo.2017.09.009.

Walter, F., Amann, F., Kos, A., Kenner, R., Phillips, M., Preux, A.D., *et al*. (2020) Direct observations of a three million cubic meter rock-slope collapse with almost immediate initiation of ensuing debris flows. *Geomorphology*, 351, 106933. https://doi.org/10.1016/j.geomorph.2019.106933.

Wanner, H., Salvisberg, E., Rickli, R. and Schüepp, M. (1998) 50 years of alpine weather statistics (AWS). *Meteorologische Zeitschrift*, 7(3), 99–111. https://doi.org/10.1127/metz/7/1998/99.

Zisser, N., Nover, G., Dürrast, H. and Siegesmund, S. (2007) Relationship between electrical and hydraulic properties of sedimentary rocks. *Zeitschrift der Deutschen Gesellschaft für Geowissenschaften*, 158(4), 883–894. https://doi.org/10.1127/1860-1804/2007/0158-0883.